Nanoparticle dispersion in porous media: Effects of array geometry and flow orientation

Deepak Mangal, Jeremy C. Palmer, and Jacinta C. Conrad

Phys. Rev. E **104**, 015102 — Published 6 July 2021

DOI: 10.1103/PhysRevE.104.015102

Nanoparticle dispersion in porous media: Effects of array geometry and flow orientation

Deepak Mangal, Jeremy C. Palmer,* and Jacinta C. Conrad†
Department of Chemical and Biomolecular Engineering, University of Houston, Houston, Texas, USA

We investigate the effects of array geometry and flow orientation on transport of finite-sized particles in ordered arrays using Stokesian dynamics simulations. We find that quiescent diffusion is independent of array geometry over the range of volume fraction of the nanoposts examined. Longitudinal dispersion under flow depends on the direction of incident flow relative to the array lattice vectors. Taylor-Aris behavior is recovered for flow along the lattice directions, whereas a non-monotonic dependence of the dispersion coefficient on the Péclet number is obtained for flow orientations slightly perturbed from certain lattice vectors, owing to a competition between directional locking and spatial velocity variations.

I. INTRODUCTION

Understanding the transport of nanoparticles through geometrically complex porous media has implications for many industrial and natural processes, including oil recovery [1], drug delivery [2, 3], the dispersion of nutrients, minerals, and contaminants through soils [4–6], and separations using techniques such as gel electrophoresis [7] and chromatography [8]. One key aspect influencing nanoparticle transport is the nature of their interactions with the surrounding medium, which include steric repulsions, van der Waals and depletion-induced attractions, and hydrodynamic and electrostatic forces. The effects of these interactions on transport behavior are strongly influenced by the structure of the porous medium and become most pronounced in strong confinement, when characteristic length scales within the porous medium, such as the pore or throat diameter, are comparable to the nanoparticle size [9–17]. Improved understanding of how the structure of the porous medium influences these interactions and, hence, nanoparticle dispersion is critical to developing strategies to control particle transport in a variety of practical settings.

Although the finite size of nanoparticles likely influences their transport in highly confined media, theoretical and computational studies of pore-scale transport have primarily focused on the transport of infinitesimal tracers. Previous studies have examined the effects of different physical factors, including flow conditions [18–21], local packing geometry [18, 19], and pore shape [21], on the dispersion of tracers. Because the tracer particles in these studies are infinitesimally sized, however, their physical interactions with the medium do not play an important role in the dispersion. Thus, there remains a need to understand the effect of these physical interactions on the transport of finite-sized particles in strongly confined porous media. Two seminal studies used Stokesian dynamics (SD) simulations to investigate the effects of medium configuration and particle size on transport through spatially periodic fibrous media at low Péclet numbers (Pe) [9, 10]. The global transport coefficients from the Stokesian dynamics simulations were found to be in good agreement with predictions from a less rigorous effective medium approach based on the Brinkman equation. Nonetheless, the effects of medium structure on particle dispersion have not been systematically investigated over a broad range of flow conditions and thus remain incompletely understood.

In our recent study [22], we performed SD simulations to investigate the effects of steric and hydrodynamic interactions and system dimensionality on particle transport in square nanopost arrays. Whereas both types of interactions hinder particle diffusion under quiescent conditions, they were found to enhance longitudinal particle dispersion under flow. We also found that longitudinal dispersion is similar in two- and three-dimensional models of nanopost arrays. Here, we extend our previous work by employing SD to examine the effects of array structure and flow orientation in similar systems. Specifically, we compare particle diffusion and dispersion in three-dimensional square and hexagonal arrays over a broad range of flow rates and orientations. We find that quiescent diffusion decreases as the volume fraction of nanoposts is increased, as expected, and is approximately independent of array geometry for the systems examined. Dispersion under flow depends on the direction of the incident flow relative to the array lattice vectors. For flow oriented along the lattice vectors, the longitudinal dispersion coefficient approximately recovers Taylor-Aris scaling behavior at high Pe. For other orientations, however, the qualitative behavior of the longitudinal dispersion coefficient depends on the nanopost volume fraction and flow angle. Notably, at large nanopost volume fractions (strong confinement), we observed non-monotonic dependence of the longitudinal dispersion coefficient on Pe when the flow orientation is slightly perturbed from certain lattice vectors. This intriguing behavior is found to arise from a competition between the directional locking of particle trajectories onto single lattice vectors caused by non-hydrodynamic interactions

* jcpalmer@uh.edu
† jcconrad@uh.edu

with the nanoposts [23], and increased spatial variations in the fluid velocity at high Pe, which act to diminish and enhance longitudinal dispersion, respectively.

II. METHODS

To investigate the effects of packing arrangement and flow orientation on particle transport, we performed SD simulations of three-dimensional square and hexagonal arrays of nanoposts. For convenience, the model systems and analyses are described by employing a set of dimensionless units in which the diameter of the transported particle d_p and $k_\mathrm{B}T$ are defined as the fundamental measures of length and energy, respectively, where k_B is Boltzmann's constant and T is temperature. The diffusive time scale $\tau_\mathrm{d} = 3\pi\eta d_\mathrm{p}^3/4k_\mathrm{B}T$ is used as the measure of time, where η is the dynamic fluid viscosity. Hence, $d_\mathrm{p} = k_\mathrm{B}T = \tau_\mathrm{d} = 1$ in the adopted units.

Each nanopost was modeled as an immobile chain of 20 tangential spheres of diameter $d_\mathrm{np} = 1$. To construct the arrays, the chains were arranged on periodic square (Fig. 1(a)) and hexagonal (Fig. 1(b)) lattices in the $x-y$ plane, with their major axes aligned along the z-direction of the simulation cell. The solid volume fraction ϕ for square and hexagonal arrays is $\phi = \pi d_\mathrm{np}^2/6\mathrm{L}^2$ and $\phi = \pi d_\mathrm{np}^2/3\sqrt{3}\mathrm{L}^2$, respectively, where L is the lattice spacing. Similar nanopost models have been employed in previous SD studies of confined particle transport [9–12, 17, 22]. In our study, we used 3×3 arrays, which was found in our previous work [22] to be sufficiently large to minimize well-known finite size effects associated with the periodicity of the systems [17, 24–26].

Pressure-driven flow through the arrays was mimicked by imposing a uniform suspension velocity $\mathbf{V}_\infty = V_\infty \mathbf{r}|\mathbf{r}|^{-1}$, where V_∞ is the magnitude and $\mathbf{r}$ is a vector specifying the direction of the flow. The flow orientation $\theta = \arccos\left(\frac{\mathbf{V}_\infty \cdot \mathbf{a}}{|\mathbf{V}_\infty||\mathbf{a}|}\right)$ is defined relative to the lattice vector $\mathbf{a}$ running parallel to the x-axis of the simulation cell (Fig. 1). For clarity, we classify the relative orientations based on the characteristic type of flow pattern they produce. Lattice orientations θ_l correspond to cases where $\mathbf{r} = n_1\mathbf{a} + n_2\mathbf{b}$ for $n_i \in \mathbb{Z}$ such that it lies along an integer linear combination of the lattice vectors $\mathbf{a}$ and $\mathbf{b}$. These orientations produce flow patterns characterized by streamlines that have a periodicity commensurate with an integer number of unit cells (Fig. 2). All other cases for $\mathbf{r}$ are classified as non-lattice orientations θ_nl and generate flow patterns with aperiodic streamlines (Fig. 2). In our simulations, we examined a variety of lattice and non-lattice orientations ranging from $0^\circ - 45^\circ$ and $0^\circ - 30^\circ$ for the square and hexagonal array, respectively.

The simulations were conducted under dilute conditions by considering the transport of a single particle through the nanopost arrays. Particle trajectories were propagated using the SD algorithm described in our previous study [22], employing a integration time step $\mathrm{d}t$ in the range of $10^{-7} - 10^{-5}$ depending on the value of V_∞. For large V_∞, an appropriate time step was identified by choosing $\mathrm{d}t$ such that displacements due to diffusion and advection were on the same order (i.e. $\sqrt{2k_\mathrm{B}T\mathrm{d}t/3\pi\eta d_\mathrm{p}} \sim V_\infty \mathrm{d}t$). In each case, additional tests were performed to confirm that computed transport properties were insensitive to further reduction of $\mathrm{d}t$ ($< 3\%$ variation). Hydrodynamic interactions between the diffusing particle and nanoposts were rigorously modeled by including both far-field and near-field components. Far-field hydrodynamic interactions were treated using the Ewald summation method [17, 24–26]. To prevent unphysical overlaps, hard-sphere excluded volume interactions between the diffusive particle and nanoposts were modeled using the standard rejection scheme [12, 17]. All other details of the SD simulations are identical to those reported in ref. [22].

Transport properties were computed by averaging over an ensemble of 100 independent particle trajectories, and statistical uncertainties were estimated from the standard error of the mean. Particle transport under quiescent conditions was characterized by computing the diffusivity from the long-time limit of the ensemble-averaged, in-plane mean-square displacement (MSD), $D_\mathrm{q} = \lim_{\Delta t \to \infty} \left\langle \Delta r^2(\Delta t) \right\rangle / 4\Delta t$. Similarly, particle transport under flow conditions was characterized by computing the asymptotic longitudinal dispersion coefficient (dispersion in the direction of flow) D_L [27, 28]:

$$D_\mathrm{L} \equiv \lim_{t \to \infty} \frac{1}{2} \frac{d\sigma_\mathrm{L}^2(t)}{dt}, \tag{1}$$

where $\sigma_\mathrm{L}^2(t) = \left\langle (\Delta r_\mathrm{L}(t) - \langle V_\mathrm{L} \rangle t)^2 \right\rangle$ is the particle MSD evaluated in the frame of reference of the average longitudinal velocity $\langle V_\mathrm{L} \rangle$. The velocity $\langle V_\mathrm{L} \rangle$ was estimated from a linear fit to the average particle displacements over time. We normalize D_q and D_L by the diffusivity of the freely-diffusive particle $D_0 = k_\mathrm{B}T/3\pi\eta d_\mathrm{p}$.

III. RESULTS AND DISCUSSION

We first examined the particle diffusivity under quiescent conditions in both array types as a function of the solid volume fraction ϕ (Fig. 3). As expected, the normalized diffusivity D_q/D_0 decreases monotonically with increasing ϕ, dropping to approximately 50% of the free diffusivity D_0 as ϕ is increased from 0 to 0.058. This behavior reflects the slowing of particle dynamics due to increasing steric hindrance and hydrodynamic drag from the nanoposts as the solid volume fraction is increased. The particle diffusivities in the square and hexagonal arrays with the same ϕ are nearly indistinguishable, indicating that the quiescent dynamics are insensitive to the differences in array

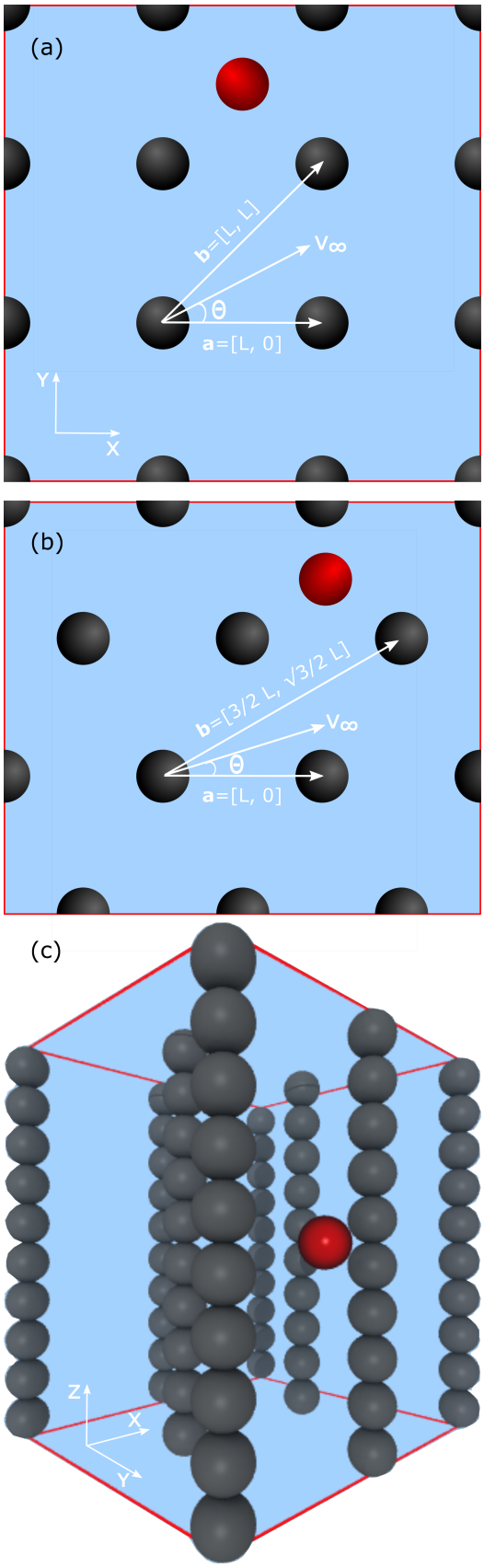

FIG. 1. Two-dimensional orthographic projection of the (a) square and (b) hexagonal nanopost arrays in the $x-y$ plane of the simulation cell. (c) Three dimensional perspective view of a section of a hexagonal nanopost array. The spheres representing the nanoposts (grey, np) and the diffusing particle (red, p) have the same diameter (i.e., $d_{\mathrm{np}} = d_{\mathrm{p}}$).

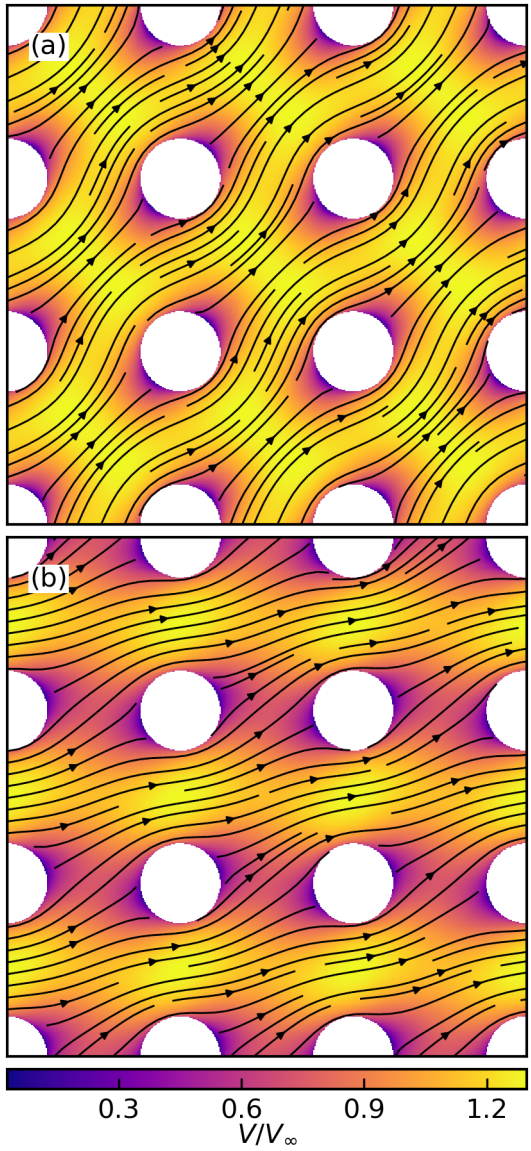

FIG. 2. Streamlines for (a) lattice ($\theta_l = 45^\circ$) and (b) non-lattice ($\theta_{nl} = 20^\circ$) flow orientations in square arrays with $\phi = 0.028$.

geometry for the two types of systems considered here. These findings are consistent with previous smooth particle hydrodynamics simulations, which show that the diffusivity of infinitesimal tracers is nearly independent of geometry in spatially periodic porous media with $\phi = 0.4$ (porosity of 0.6) [29]. Thus, for both finite-sized particle and tracers, simulations suggest that ϕ, which determines the effective degree of confinement, is the dominant factor controlling particle transport under quiescent conditions.

Particle transport under flow conditions was investigated by simulating systems with $\phi = 0.028$ and 0.058 for each array geometry. The behavior of the normalized average particle velocity $\langle V_{\mathrm{L}} \rangle / V_\infty$ as a function of flow orientation θ (Fig. 4) depends

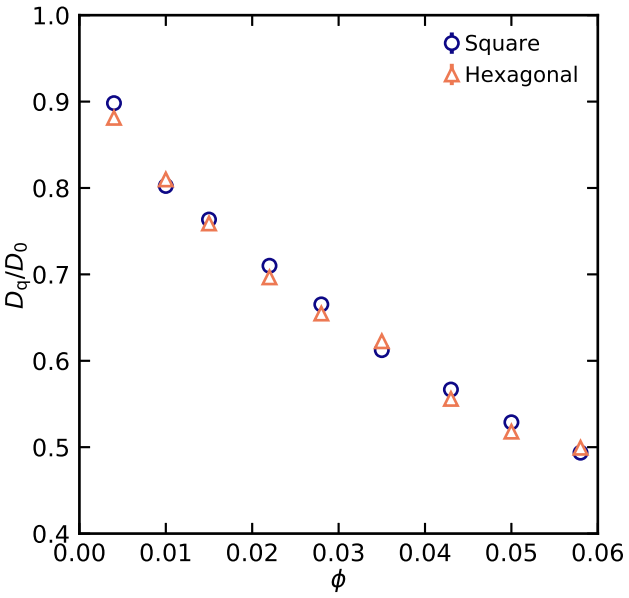

FIG. 3. Normalized in-plane diffusion coefficients D_q/D_0 as functions of nanopost volume fraction ϕ in square (circles) and hexagonal (triangles) arrays. Estimated uncertainties are smaller than the symbol sizes.

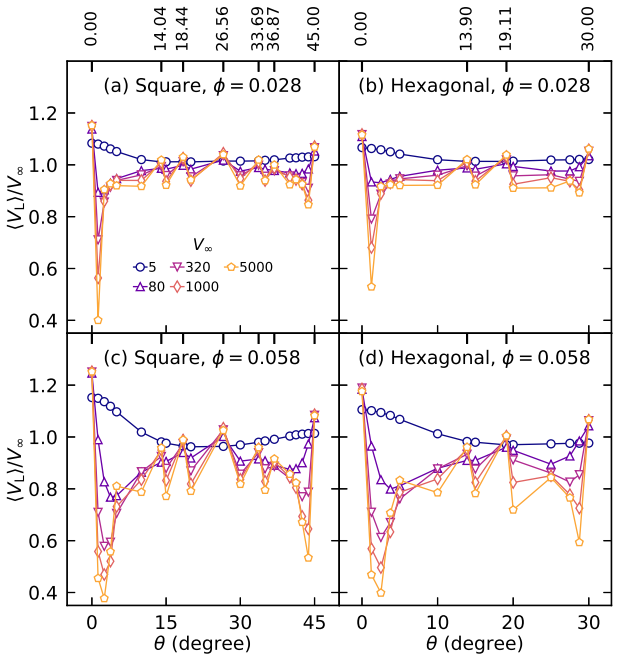

FIG. 4. Normalized average particle velocities $\langle V_L \rangle / V_\infty$ as functions of flow orientation θ in (a,c) square and (b,d) hexagonal arrays with $\phi = 0.028$ (top row) and $\phi = 0.058$ (bottom row). The lattice orientations θ_l are indicated on the top y-axis in panels (a, b).

on the relative importance of advective and diffusive particle transport characterized by the dimensionless Péclet number $\mathrm{Pe} = \langle V_L \rangle d_p / D_0$. For uniform flow velocity $V_\infty = 5$ ($\mathrm{Pe} \lesssim 10$), advective and diffusive particle transport mechanisms compete. In this case, $\langle V_L \rangle / V_\infty$ attains a maximum for the lattice orientation $\theta_l = 0°$ and then gradually decreases and becomes almost constant as θ increases. As V_∞ and hence Pe increase, advection becomes dominant and the behavior of $\langle V_L \rangle / V_\infty$ becomes increasingly sensitive to changes in θ. For $V_\infty > 5$ ($\mathrm{Pe} > 10$), $\langle V_L \rangle / V_\infty$ exhibits local maxima for lattice orientations θ_l that yield periodic flow patterns (Fig. 4(a),(b)). The particle velocity decreases as the incident flow is perturbed away from these orientations. In particular, slight deviations from orientations along one of the primitive lattice vectors $\{\mathbf{a}, \mathbf{b}\}$ lead to precipitous drops in $\langle V_L \rangle / V_\infty$ that become more prominent as V_∞ increases. Increasing the solid volume fraction from $\phi = 0.028$ to 0.058 also markedly enhances the sensitivity of $\langle V_L \rangle / V_\infty$ to changes in θ (Fig. 4 (c),(d)). The local maxima of the average velocity for lattice orientations θ_l at large flow rates is in agreement with earlier Brownian dynamics simulations of DNA electrophoresis through tilted hexagonal post arrays [30] and molecular dynamics simulations of finite-sized particles through a regular lattice of cylindrical obstacles [31].

The variation of average velocity with flow orientation at large V_∞ arises from changes in the frequency of particle collisions with the nanoposts, which slow the motion of the particles. The mean collision frequency $\langle C \rangle$ (the average number of collisions per unit distance travelled) decreases with increasing V_∞ for lattice flow orientations θ_l (not shown), leading to faster transport through the nanopost array [30]. By contrast, the collision frequency increases or remains nearly constant with increasing V_∞ for non-lattice flow orientations θ_{nl}, leading to a decrease in $\langle V_L \rangle / V_\infty$ [30].

The most pronounced decreases in $\langle V_L \rangle / V_\infty$ occur when the flow is slightly perturbed from θ_l orientations along the primitive lattice vectors ($\{0°, 45°\}$ and $\{0°, 30°\}$ for square and hexagonal array, respectively) (Fig. 4). These abrupt decreases arise due to directional locking, in which particle dynamics become dominated by advection along a specific vector over a finite range of θ [23]. To visualize this directional locking behavior, we computed the log-probability density distribution of the particle positions in the $x - y$ plane $\log_{10} P(x, y)$ for selected flow orientations θ at $V_\infty = 1000$ (Figs. 5 and 6). When the flow is oriented along $\mathbf{a}$ or $\mathbf{b}$, particles are able to advect along unobstructed paths through the void spaces between the rows of nanoposts. When the flow direction is slightly perturbed from either of these directions (e.g., $\{1.25°, 43.75°\}$ and $\{1.25°, 28.75°\}$ for square and hexagonal arrays, respectively), however, the particle trajectories become locked along one of the lattice vectors, resulting in frequent (periodic) collisions with the nanoposts that decrease their velocity. Indeed, for a flow orientation of $\theta_{nl} = 1.25°$ in square and

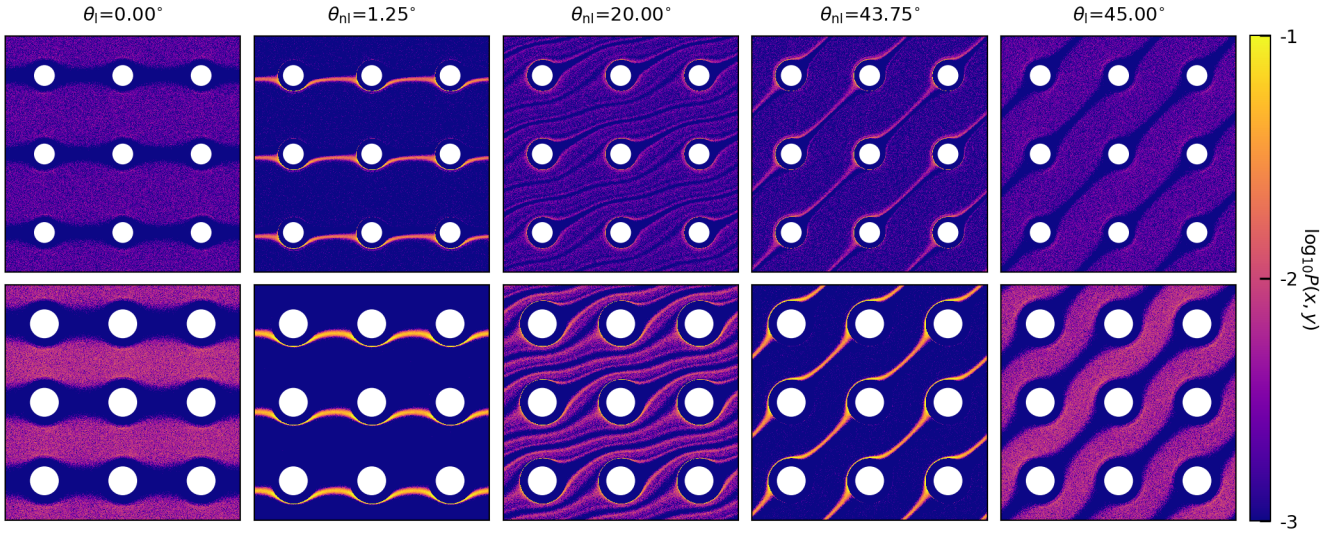

FIG. 5. Log-probability density distributions of particle positions $\log_{10} P(x, y)$ for different flow orientations θ in square arrays at $V_\infty = 1000$ for $\phi = 0.028$ (top row) and $\phi = 0.058$ (bottom row). The intense blue color corresponds to the value $\log_{10} P(x, y) < -3$.

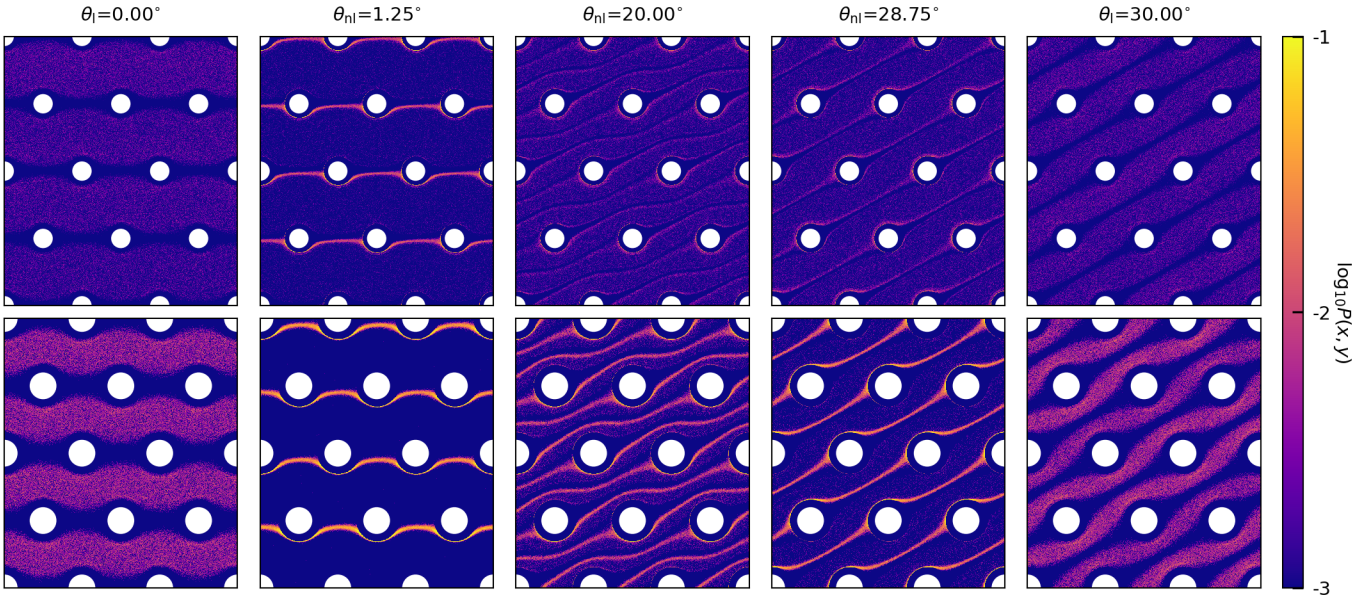

FIG. 6. Log-probability density distributions of particle positions $\log_{10} P(x, y)$ for different flow orientations θ in hexagonal arrays at $V_\infty = 1000$ for $\phi = 0.028$ (top row) and $\phi = 0.058$ (bottom row). The intense blue color corresponds to the value $\log_{10} P(x, y) < -3$.

hexagonal arrays with $\phi = 0.058$, we observe "perfect" directional locking, in which all particles move closely along the lattice vector **a** (See Movies S1 and S2 in Supplemental Material [32]). In this case, the particles advect towards the centers of nanoposts, leading to frequent, direct collisions and a concomitant decrease in $\langle V_L \rangle / V_\infty$ as V_∞ increases (Fig. 4(c),(d)).

We also examined the normalized longitudinal dispersion coefficient D_L/D_0 (along the direction of flow) as a function of flow angle θ for different values of the imposed uniform fluid velocity V_∞ (Fig. 7). For $V_\infty = 5$, D_L/D_0 is maximum at $\theta_l = 0°$, but decreases slightly (by less than an order of magnitude) with increasing θ. As advection becomes increasingly dominant at larger V_∞, however, the sensitivity of D_L/D_0 to flow orientation increases markedly, varying by as much as

4 orders of magnitude with θ at the largest velocity ($V_\infty = 5000$) examined. In the advection dominated regime ($V_\infty > 5$, Pe > 10), D_L/D_0 exhibits local maxima for lattice flow orientations θ_l (Fig. 7 (a),(b)) and decreases as θ is perturbed away from these orientations. Similar general trends are observed at both solid volume fractions examined, except for the appearance of new local extrema for $V_\infty > 80$ at flow orientations slightly perturbed from θ_l orientations along **a** or **b** in the systems with $\phi = 0.058$ (Fig. 7 (c),(d); near $\{1.25°, 43.75°\}$ and $\{1.25°, 28.75°\}$ for square and hexagonal arrays, respectively). The strong dependence of the longitudinal dispersion coefficient on flow orientation at large V_∞ is in contrast with an earlier simulation study of the transport of infinitesimal tracers through two-dimensional square nanopost arrays at Pe $= 10^2$, which reported a sharp decrease in D_L upon increasing θ over the range $0 - 10°$ and a wide plateau region for $\theta = 15 - 45°$ [33].

The sensitivity of D_L/D_0 to flow angles at large V_∞ arises due to the interplay between flow streamlines and particle collisions with the nanoposts. For lattice flow orientations θ_l, periodicity of the streamlines results in channel-like flow between the rows of nanoposts on sufficiently large length scales. With the emergence of channel-like flow, the longitudinal dispersion coefficient is expected to increase rapidly with increasing V_∞ and eventually recover Taylor-Aris dispersion behavior at sufficiently high flow velocities. For non-lattice orientations θ_{nl}, however, the flow streamlines are aperiodic and direct particles to collide more frequently with the nanoposts, leading to slower dynamics. As a result, D_L/D_0 increases more slowly with increasing V_∞ for θ_{nl} compared to periodic flow orientations θ_l.

Consistent with these expectations, the correlation between D_L/D_0 and the normalized (dimensionless) mean collision frequency $\langle C \rangle d_p$ exhibits distinct trends for the two types of flow orientations (Fig. 8). For θ_l, the collision frequency decreases and longitudinal dispersion increases sharply with increasing V_∞. By contrast, for θ_{nl}, the collision frequency increases or remains approximately constant and longitudinal dispersion increases more slowly with V_∞.

Particle dispersion arises from a combination of advection and diffusion at the pore scale [34]. Thus, we also examined the behavior of D_L/D_0 with its natural dimensionless scaling variable, the Péclet number Pe. For θ_l orientations along **a** or **b** in square arrays with $\phi = 0.028$, D_L/D_0 exhibits a gradual initial increase and then crosses over to $\propto$Pe^n scaling with $n \approx 2$ at Pe~ 10. (Fig. 9(a)). The recovery of Taylor-Aris behavior (i.e., quadratic scaling with Pe) at Pe> 10, where advection is the dominant transport mechanism, is in accord with earlier theoretical [20] and simulation [18, 19, 33] studies of tracer dispersion in periodic ordered media. For other lattice orientations θ_l, Taylor-Aris behavior is observed at high Pe, but the crossover to quadratic scaling is delayed to Pe≈ 500 (Fig. 9(a)). Similar qualitative behavior is also observed in the square arrays with $\phi = 0.058$, but

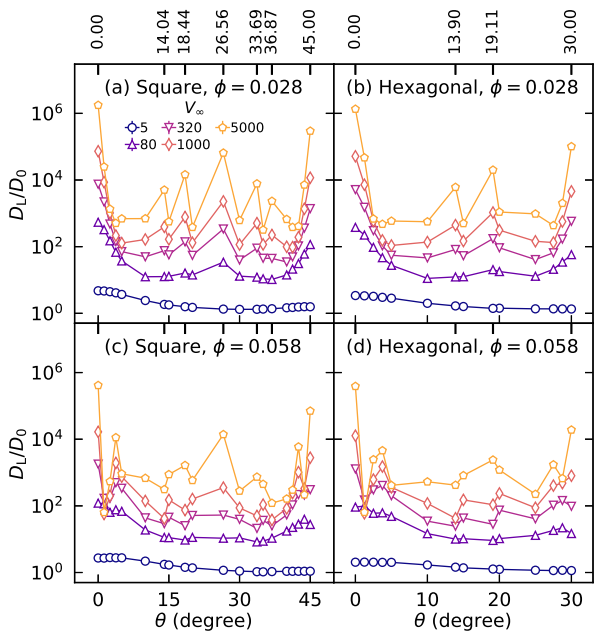

FIG. 7. Normalized longitudinal dispersion coefficients D_L/D_0 as functions of flow orientation θ in (a,c) square and (b,d) hexagonal arrays with $\phi = 0.028$ (top row) and $\phi = 0.058$ (bottom row). The lattice orientations θ_l are indicated on the top y-axis in panels (a, b).

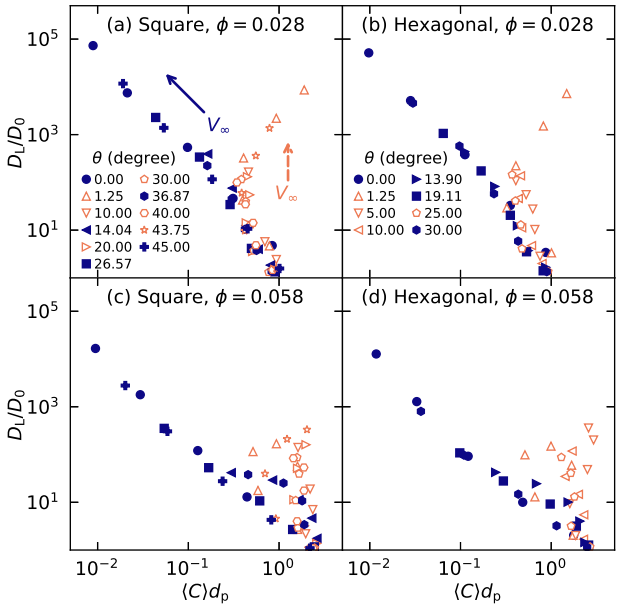

FIG. 8. Correlations between normalized longitudinal dispersion coefficient D_L/D_0 and average normalized collision frequency $\langle C \rangle d_p$ in (a,c) square and (b,d) hexagonal arrays with $\phi = 0.028$ (top row) and $\phi = 0.058$ (bottom row). Open and closed symbols denote non-lattice θ_{nl} and lattice θ_l directions, respectively. The solid and dashed line arrows in (a) show the trend with increasing V_∞ for lattice directions θ_l and non-lattice directions θ_{nl}, respectively.

the magnitude of D_L/D_0 is decreased (Fig. 9(c)). This behavior arises because the distribution of streamlines that are sterically accessible to the center of the particles becomes increasingly narrow with increasing ϕ [22].

By contrast, qualitatively different trends are observed for the non-lattice flow orientations θ_{nl}. Notably, for the arrays with $\phi = 0.028$, D_L/D_0 exhibits an intermediate regime with $\propto \mathrm{Pe}^n$ scaling with $1 < n < 2$ before turning down at $\mathrm{Pe} \gtrsim 10^3$ (Fig. 9(b)). For $\theta_{nl} = \{1.25°, 43.75°\}$, which are slightly perturbed from orientations along the primitive lattice vectors $\{\mathbf{a}, \mathbf{b}\}$, increasing ϕ from 0.028 to 0.058 shifts the downturn to lower Pe and results in the emergence of non-monotonic behavior and a second power-law regime at $\mathrm{Pe} > 5 \times 10^3$ (Fig. 9(b),(d)). This non-monotonic behavior results from two competing effects. As Pe increases, directional locking becomes increasingly pronounced for these flow orientations, narrowing the distributions of streamlines sampled by the particles, which acts to decrease particle dispersion. Increasing Pe, however, also leads to larger spatial variations of the fluid velocity throughout the nanopost arrays, which enhances dispersion. The latter effect ultimately dominates, leading to a second power-law regime at sufficiently high Pe.

Longitudinal dispersion in the hexagonal arrays is qualitatively similar (Fig. 10) to that in the square arrays, including the presence of non-monotonic behavior (or pronounced plateaus) at $\phi = 0.058$ for orientations $\theta_{nl} = \{1.25°, 28.75°\}$ that are slightly perturbed from the lattice vectors $\{\mathbf{a}, \mathbf{b}\}$, where strong directional locking is observed. At the same ϕ and Pe for $\theta_l = 0°$, however, D_L/D_0 is slightly larger in the square arrays. This small disparity is due to the fact that the spacing between rows in the square arrays is slightly larger, allowing the centers of the particles to access a broader distribution of streamlines.

Our findings are at odds with an earlier theoretical study of tracers in periodic ordered arrays [20], which predicted that D_L/D_0 is independent of Pe for non-lattice flow orientations. The presence of a downturn followed by a second power-law regime for $\phi = 0.058$ and $\theta_{nl} = \{1.25°, 43.75°\}$ is consistent with the behavior observed in a computational study of tracer transport through two-dimensional square arrays [18]. In that study, however, the qualitative behavior of D_L/D_0 was found to be insensitive to θ for several flow orientations between 0 and 45° and no non-monotonic behavior was observed. Additionally, we observe that dispersion decreases in both array types as ϕ increases, whereas previous studies report the opposite behavior for tracers in square arrays [19]. Although the cause for the discrepancy between our results and those reported in these previous studies [18–20] is unclear, we posit that it may be due to the use of finite-sized particles rather than tracers in our study. This hypothesis is supported by simulations showing that D_L/D_0 increases monotonically with Pe for particles of a smaller relative size ($d_p = d_{np}/5$ at the same $\phi = 0.058$ and flow orientation $\theta_{nl} = 1.25°$, not shown). This result is qualitatively consistent with the previous study of infinitesimal tracers [18], but additional studies are needed to fully understand the effects of particle size on dispersion behavior.

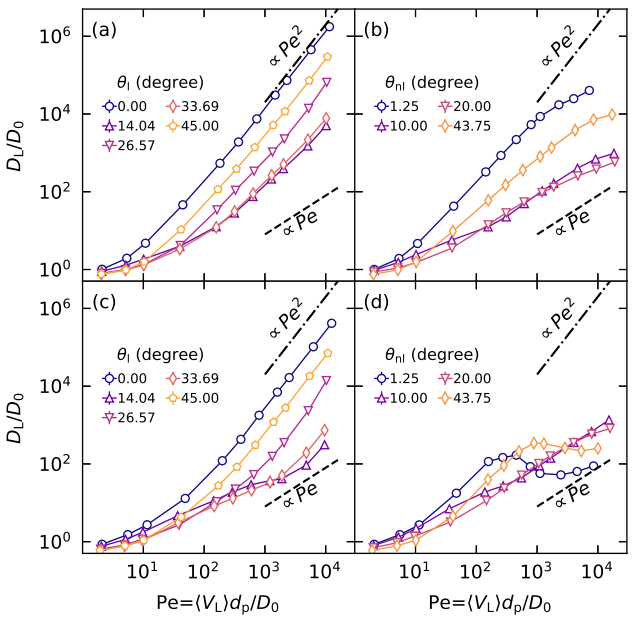

FIG. 9. Normalized longitudinal dispersion coefficients D_L/D_0 as functions of Péclet number Pe in square arrays with $\phi = 0.028$ (top row) and $\phi = 0.058$ (bottom row) for (a,c) θ_l and (b,d) θ_{nl} flow orientations.

IV. CONCLUSIONS

We performed Stokesian dynamics simulations to study the effects of array geometry and flow orientation on the transport on finite-sized particles through square and hexagonal nanopost arrays. Under quiescent conditions, the particle diffusivity D_0 decays monotonically upon increasing the nanopost volume fraction ϕ due to enhanced steric hindrance and hydrodynamic drag in strong confinement, but is independent of the array geometry over the range of ϕ investigated. Under flow, the behavior of the normalized longitudinal dispersion coefficient D_L/D_0 depends on the direction of incident flow relative to the lattice vectors. For lattice flow orientations θ_l, D_L/D_0 exhibits asymptotic scaling behavior (i.e., quadratic scaling) at large Pe consistent with Taylor-Aris dispersion. For non-lattice flow orientations θ_{nl}, however, the scaling behavior of D_L/D_0 is strongly influenced by both ϕ and flow direction. Specifically, we observe non-monotonic dependence of D_L/D_0 on Pe for flow angles slightly perturbed away from the primitive lattice vectors $\{\mathbf{a}, \mathbf{b}\}$ for large ϕ owing to the competition between directional locking and spatial variations in fluid velocity.

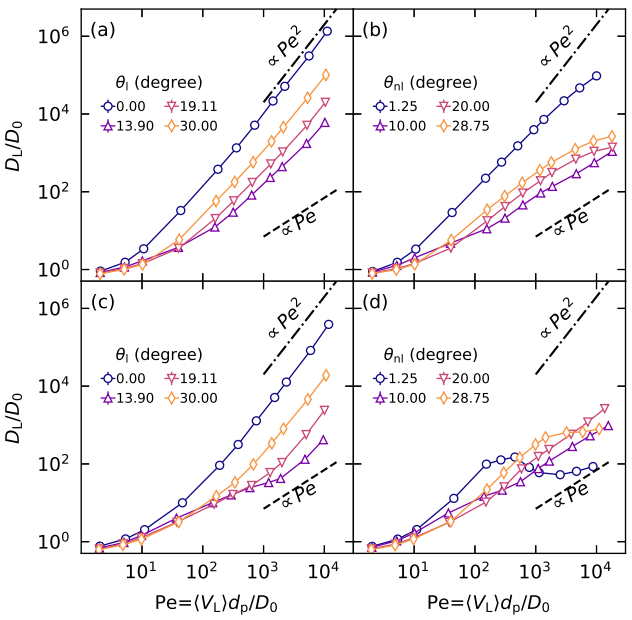

FIG. 10. Normalized longitudinal dispersion coefficients D_L/D_0 as functions of Péclet number Pe in hexagonal arrays with $\phi = 0.028$ (top row) and $\phi = 0.058$ (bottom row) for (a,c) θ_l and (b,d) θ_{nl} flow orientations.

The simulations in this study provide insights into the effects of array geometry and flow direction on the transport of finite-size particles in ordered arrays, similar to those used in separations techniques such as deterministic lateral displacement [35, 36] and hydrodynamic chromatography [37–39]. Although we only included purely repulsive steric interactions between the particles and nanoposts in our models, other types of interactions including van der Waals, electrostatic, and depletion forces may also be present in many applied settings. Additionally, there may be variability in nanopost size and spacing in experimental systems, resulting in deviations from the perfectly ordered arrays considered here. Nonetheless, the effects of different types of particle-nanopost interactions and structural defects on particle dispersion through nanopost arrays remain incompletely understood. We anticipate that the computational techniques and models employed in this study can be adapted to address these open questions in future work.

[1] H. ShamsiJazeyi, C. A. Miller, M. S. Wong, J. M. Tour, and R. Verduzco, Journal of Applied Polymer Science **131**, 40576 (2014).
[2] M. Vallet-Regí, M. Colilla, I. Izquierdo-Barba, and M. Manzano, Molecules **23**, 47 (2017).
[3] F.-Y. Kong, J.-W. Zhang, R.-F. Li, Z.-X. Wang, W.-J. Wang, and W. Wang, Molecules **22**, 1445 (2017).
[4] W. Tungittiplakorn, C. Cohen, and L. W. Lion, Environmental Science & Technology **39**, 1354 (2005).
[5] M. Naveed, L. K. Brown, A. C. Raffan, T. S. George, A. G. Bengough, T. Roose, I. Sinclair, N. Koebernick, L. Cooper, C. A. Hackett, and P. D. Hallett, European Journal of Soil Science **68**, 806 (2017).
[6] I. C. Ossai, A. Ahmed, A. Hassan, and F. S. Hamid, Environmental Technology & Innovation **17**, 100526 (2020).
[7] M. Zarei, M. Zarei, and M. Ghasemabadi, TrAC Trends in Analytical Chemistry **86**, 56 (2017).
[8] B. W. J. Pirok, N. Abdulhussain, T. Aalbers, B. Wouters, R. A. H. Peters, and P. J. Schoenmakers, Analytical Chemistry **89**, 9167 (2017).
[9] R. J. Phillips, W. M. Deen, and J. F. Brady, AIChE Journal **35**, 1761 (1989).
[10] R. J. Phillips, W. M. Deen, and J. F. Brady, Journal of Colloid and Interface Science **139**, 363 (1990).
[11] T. Stylianopoulos, M.-Z. Poh, N. Insin, M. G. Bawendi, D. Fukumura, L. L. Munn, and R. K. Jain, Biophysical Journal **99**, 1342 (2010).
[12] T. Stylianopoulos, B. Diop-Frimpong, L. L. Munn, and R. K. Jain, Biophysical Journal **99**, 3119 (2010).
[13] K. He, F. B. Khorasani, S. T. Retterer, D. K. Thomas, J. C. Conrad, and R. Krishnamoorti, ACS Nano **7**, 5122 (2013).
[14] K. He, S. T. Retterer, B. R. Srijanto, J. C. Conrad, and R. Krishnamoorti, ACS Nano **8**, 4221 (2014).
[15] J. D. C. Jacob, K. He, S. T. Retterer, R. Krishnamoorti, and J. C. Conrad, Soft Matter **11**, 7515 (2015).
[16] J. D. C. Jacob, R. Krishnamoorti, and J. C. Conrad, Physical Review E **96**, 022610 (2017).
[17] J. Hansing and R. R. Netz, Macromolecules **51**, 7608 (2018).
[18] H. P. A. Souto and C. Moyne, Physics of Fluids **9**, 2253 (1997).
[19] D. Edwards, M. Shapiro, H. Brenner, and M. Shapira, Transport in Porous Media **6**, 337 (1991).
[20] D. L. Koch, R. G. Cox, H. Brenner, and J. F. Brady, Journal of Fluid Mechanics **200**, 173 (1989).
[21] R. S. Maier, Philosophical Transactions of the Royal Society of London. Series A: Mathematical, Physical and Engineering Sciences **360**, 497 (2002).
[22] D. Mangal, J. C. Conrad, and J. C. Palmer, AIChE Journal **67**, e17147 (2021).
[23] J. Frechette and G. Drazer, Journal of Fluid Mechanics **627**, 379 (2009).
[24] J. F. Brady and G. Bossis, Annual Review of Fluid Mechanics **20**, 111 (1988).
[25] R. J. Phillips, J. F. Brady, and G. Bossis, Physics of Fluids **31**, 3473 (1988).
[26] M. Wang and J. F. Brady, The Journal of Chemical Physics **142**, 094901 (2015).
[27] R. S. Maier, D. M. Kroll, R. S. Bernard, S. E. Howington, J. F. Peters, and H. T. Davis, Physics of Fluids **12**, 2065

(2000).
[28] M. P. Howard, A. Gautam, A. Z. Panagiotopoulos, and A. Nikoubashman, Physical Review Fluids **1**, 044203 (2016).
[29] Y. Zhu and P. J. Fox, Transport in Porous Media **43**, 441 (2001).
[30] Z. Chen and K. D. Dorfman, Electrophoresis **35**, 405 (2013).
[31] J. Koplik and G. Drazer, Physics of Fluids **22**, 052005 (2010).
[32] See Supplemental Material at `URLwillbeinsertedbypublisher` for particle trajectory movies at different flow orientations in square array.
[33] J. Salles, J. F. Thovert, R. Delannay, L. Prevors, J. L. Auriault, and P. M. Adler, Physics of Fluids A: Fluid Dynamics **5**, 2348 (1993).
[34] D. Hlushkou, S. Piatrusha, and U. Tallarek, Physical Review E **95**, 063108 (2017).
[35] L. R. Huang, E. C. Cox, R. H. Austin, and J. C. Sturm, Science **304**, 987 (2004).
[36] J. McGrath, M. Jimenez, and H. Bridle, Lab Chip **14**, 4139 (2014).
[37] J. O. de Beeck, W. D. Malsche, P. D. Moor, and G. Desmet, Journal of Separation Science **35**, 1877 (2012).
[38] A. Daneyko, D. Hlushkou, S. Khirevich, and U. Tallarek, Journal of Chromatography A **1257**, 98 (2012).
[39] A. M. Striegel and A. K. Brewer, Annual Review of Analytical Chemistry **5**, 15 (2012).